To appear in Proc. of the inaugural ICREA Workshop on
"The High-Energy Emission from Pulsars and their Systems" (2010),
eds. N. Rea & D. Torres, (Springer Astrophysics & Space Science series).

Lepton Acceleration in Pulsar Wind Nebulae

Matthew G. Baring

Abstract Pulsar Wind Nebulae (PWNe) act as calorimeters for the relativistic pair winds emanating from within the pulsar light cylinder. Their radiative dissipation in various wavebands is significantly different from that of their pulsar central engines: the broadband spectra of PWNe possess characteristics distinct from those of pulsars, thereby demanding a site of lepton acceleration remote from the pulsar magnetosphere. A principal candidate for this locale is the pulsar wind termination shock, a putatively highly-oblique, ultra-relativistic MHD discontinuity. This paper summarizes key characteristics of relativistic shock acceleration germane to PWNe, using predominantly Monte Carlo simulation techniques that compare well with semi-analytic solutions of the diffusion-convection equation. The array of potential spectral indices for the pair distribution function is explored, defining how these depend critically on the parameters of the turbulent plasma in the shock environs. Injection efficiencies into the acceleration process are also addressed. Informative constraints on the frequency of particle scattering and the level of field turbulence are identified using the multiwavelength observations of selected PWNe. These suggest that the termination shock can be comfortably invoked as a principal injector of energetic leptons into PWNe without resorting to unrealistic properties for the shock layer turbulence or MHD structure.

1 Introduction

Pulsar wind nebulae (PWNe) have fascinated astronomers ever since the discovery of the Crab Nebula. This source provides the template for PWN studies because of the excellent multiwavelength spectral information (de Jager & Harding 1992; Atoyan & Aharonian, 1996; Abdo et al. 2010b) and stunning spatial imaging afforded by radio (historic), optical (Hester et al. 1995 for *Hubble*) and X-ray (Weis-

Matthew G. Baring
Department of Physics and Astronomy, MS-108, Rice University, P. O. Box 1892,
Houston, TX 77251-1892, USA. e-mail: *baring@rice.edu*

skopf, et al. 2000 for *Chandra*) observations. Its unparalleled observational quality is driven by the exceptional powerhouse at its center, the high spin-down power Crab pulsar. The central pulsar fuels the dissipation in its surrounding PWN (exemplified in the seminal Rees & Gunn, 1974, and Kennel & Coroniti, 1984, models), with the nebula serving in a symbiotic relationship as the calorimeter for the pulsar over its entire spin-down history. Therefore, the interface between the central engine and the nebula must play a principal role in setting up the emission seen in PWNe. This boundary is the **pulsar wind termination shock** (PWTS), where the wind is abruptly slowed by the ram pressure of the circumstellar material; it forms the focus of this perspective on lepton acceleration in PWNe.

This shock is a natural site for the acceleration of particles that spawn the non-thermal radiation in PWNe that we observe. It should possess turbulent electrodynamic fields that can energize and stochastically diffuse charges extremely efficiently. Yet, the PWTS is not the only possible site for leptonic acceleration. Field reconnection in and near the quasi-equatorial current sheet between the pulsar light cylinder and the termination shock is an alternative (e.g. Lyubarsky & Kirk 2001; Kirk & Skjæraasen 2003; Pétri & Lyubarsky 2007). In compact regions such as X-points in the striped wind, magnetic reconnection can release large amounts of energy as field tension is converted to heat of particles. Such a prospect needs fuller exploration from a theoretical standpoint. Reconnection theory needs to make robust predictions of distributions and injection efficiencies (from thermal gas) of accelerated populations in order to connect effectively to PWNe observations. The understanding of shock acceleration is more developed in this regard, and accordingly is the focus of this paper. We note that the solar corona may prove a powerful testing ground for honing models of reconnection in the same way that the solar wind has demonstrated the general viability of diffusive acceleration at non-relativistic shocks. It should also be remarked that all escaping pulsar wind leptons impact the surface of the termination shock, whereas perhaps only a minority of such thread the environs of the current sheet reconnection region. Notwithstanding, reconnection in the near wind zone may contribute significantly to the evolution of the global MHD structure and associated wind parameters, as well as generate some pre-acceleration, both of which in turn influence the cumulative contribution of the PWTS as an injector to a pulsar wind nebula over its active lifetime.

This paper summarizes the key aspects of diffusive acceleration at relativistic shocks in general, and pulsar wind termination shocks in particular. As the injector of ultra-relativistic leptons, and ions, into PWNe, this process is only indirectly probed by radiation observations of nebulae. The volumetric extension of PWNe encompasses significant spatial stratification of both the nebular magnetic field and the fluid flow speed, the model template for which is the spherically symmetric Kennel & Coroniti (1984) contribution. Moreover, temporal evolution is significant, with high energy electrons cooling rapidly over the lifetime of a PWN like the Crab, driving synchrotron "burn-off" that is probed in the X-rays (see the review of Gaensler & Slane, 2006, for an extensive discussion of PWN observations and guiding interpretative material). Yet multiwavelength coverage, from radio to X-ray to high energy gamma-rays provides substantial constraints on the PWTS acceleration pro-

cess. Presuming nebular fields in the range of $B \sim 0.1\,\mathrm{mG}$ implies pair Lorentz factors in the range $\gamma_e \sim 10^9 - 10^{10}$ for the Crab to enable γ-ray synchrotron emission. Since the pulsar is unlikely to generate such energetic particles, this demands efficient acceleration at the PWTS or elsewhere. Other PWNe impose similar requirements. The PWTS energy budget divides into three components: (i) thermal downstream heat, (ii) turbulent fields, and (iii) non-thermal shock-accelerated leptons, and perhaps ions. The balance between these is not yet fully understood, though indications from plasma simulations are that these components are not widely disparate in their energy densities. The central acceleration issue for PWN studies is whether a quasi-perpendicular termination shock can generate a sufficient injection efficiency $\varepsilon_{\mathrm{inj}}$ and the right spectral index in different energy ranges. In this paper, it becomes evident that the index issue can be satisfied in global terms using the current understanding of diffusive acceleration at relativistic shocks, while more work is needed to address the injection issue in a satisfactory manner.

2 Lepton Acceleration at Relativistic Shocks

To understand the nature of relativistic lepton injection into the PWN, it is insightful to explore the general nature of particle acceleration at relativistic shocks. The key characteristic that distinguishes relativistic shocks from their non-relativistic counterparts is their inherent anisotropy of the phase space distribution function $f(\mathbf{p})$ at any position. This is due to rapid convection of particles through and downstream away from the shock, since particle speeds v are never much greater than the downstream flow speed $u_2 \sim c/3$: particle distributions never realize isotropy in either fluid or shock rest frames. This renders analytic approaches more complicated (Peacock 1981) than in non-relativistic systems. Early analytic offerings on particle acceleration at relativistic shocks focused on solutions of the diffusion-convection differential equation in the test-particle approximation (e.g., Kirk & Schneider 1987a; Heavens & Drury 1988; Kirk and Heavens 1989). These generally specialized to the limit of extremely small angle scattering (SAS, or *pitch angle diffusion*). In particular, the eigenfunction solution technique of Kirk & Schneider (1987a) was later successfully extended by Kirk et al. (2000) to the specific case of parallel, ultrarelativistic shocks, i.e. those with upstream fluid flow Lorentz factors $\Gamma_1 \gg 1$ in the shock rest frame. Kirk et al. demonstrated that as $\Gamma_1 \to \infty$, the accelerated particle distribution power-law index σ (for $dN/dp \propto p^2 f(\mathbf{p}) \propto p^{-\sigma}$) asymptotically approached a constant, $\sigma \to 2.23$, a value realized when $\Gamma_1 \gtrsim 10$. This result has been popularly invoked in astrophysics models of various sources, but is of very restricted applicability, as will become evident below. While diffusion-convection differential equation approaches are usually restricted to SAS that would be applicable to particle transport in quasi-linear field turbulence regimes, recently they have been generalized by Blasi & Vietri (2005) and Morlini, Blasi & Vietri (2007) to incorporate large angle deflections in MHD turbulence of larger amplitudes $\delta B/B$. The operating definition of such large angle scattering (LAS) is that the particle

experiences momentum deflections on typical angles $\theta_{\rm scatt} \gtrsim 1/\Gamma_1$ in interactions with MHD turbulence in the shock environs. Clearly, for ultra-relativistic shocks, LAS can be realized with quite modest deflections.

A central limitation of these analytic methods is that they are restricted to power-law regimes, which are only realized when there is no preferred momentum scale, i.e. far above the thermal injection momentum. Therefore they provide no probes of the injection efficiency $\varepsilon_{\rm inj}$ (defined to be the fraction of particles by number residing in the non-thermal tail of the distribution), how $\varepsilon_{\rm inj}$ connects key shock environmental parameters, and therefore how it correlates to the non-thermal distribution index σ. Hence the niche for Monte Carlo techniques for modeling diffusive transport in shocks. Such complementary simulation approaches have been employed for relativistic shocks by a number of authors, including test-particle analyses by Kirk & Schneider (1987b), Ellison, Jones & Reynolds (1990), and Baring (1999) for parallel, steady-state shocks, and extensions to include oblique magnetic fields by Ostrowski (1991), Ballard & Heavens (1992), Bednarz & Ostrowski (1998), Ellison & Double (2004), Niemiec & Ostrowski (2004), Stecker, Baring & Summerlin (2007) and Baring & Summerlin (2009). The Monte Carlo method successfully reproduced the asymptotic $\Gamma_1 \to \infty$ index value of $\sigma \approx 2.23$ in work by different groups (Bednarz & Ostrowski 1998; Baring 1999; Achterberg, et al. 2001; Ellison & Double 2002). There are two main types of Monte Carlo simulation on the market: those that inject prescribed field turbulence to effect diffusion of charges (e.g. Ostrowski 1991; Bednarz & Ostrowski 1998; Niemiec & Ostrowski 2004), and those that describe the diffusion by phenomenological scattering parameters (e.g. Ellison, Jones & Reynolds 1990; Ellison & Double 2004; Baring & Summerlin 2009). It is this latter variety that will form the focus in this exposition, because of its ability to survey the parameter space of acceleration characteristics in an incisive fashion.

Before outlining the essentials of the Monte Carlo technique used to generate many of the results presented here, it should be noted that there is a third popular approach to modeling particle acceleration at relativistic shocks: full plasma or particle-in-cell (PIC) simulations (e.g. Hoshino, et al. 1992; Nishikawa, et al. 2005; Medvedev, et al. 2005; Spitkovsky 2008). PIC codes compute fields generated by mobile charges, and the response of the charges to the dynamic electromagnetic fields. Accordingly they are rich in their information on shock-layer electrodynamics and turbulence, but pay the price of intensive demands on CPUs. This presently limits them to exploration of thermal and suprathermal energies, so that full plasma simulations generally exhibit largely Maxwellian distributions (Hoshino, et al. 1992; Nishikawa et al. 2005; Medvedev, et al. 2005). However, we note the isolated recent suggestion (Spitkovsky 2008; Martins et al. 2009; Sironi & Spitkovsky 2009) of non-thermal tails spanning relatively limited range of energies, generated by diffusive transport in PIC simulations, with the thermal population still dominating the high-energy tail by number. To interface with astrophysical spectral data, a broad dynamic range in momenta is desirable, and this is the natural niche of Monte Carlo simulation techniques.

2.1 The Monte Carlo Method

As informative background to the ensuing results on relativistic planar shocks, the structure of the simulation used to calculate diffusive acceleration is now described. It is a kinematic Monte Carlo technique that has been employed extensively in supernova remnant and heliospheric contexts, and is described in detail in numerous papers (e.g. Ellison, Jones and Reynolds, 1990, hereafter EJR90; Jones & Ellison 1991; Ellison & Double 2004; Baring & Summerlin 2009). It is conceptually similar to Bell's (1978) test particle approach to diffusive shock acceleration, and essentially solves a Boltzmann transport equation for arbitrary orientations of the large scale MHD field **B**. The background fields and fluid flow velocities on either side of the shock are uniform, and the transition at the shock is defined by the standard relativistic MHD Rankine-Hugoniot conservation relations (e.g. Double et al. 2004) that depend on both the sonic and Alfvénic Mach numbers. Particles are injected upstream of the shock with a Maxwell-Boltzmann distribution of finite temperature, and convect and gyrate in the laminar electromagnetic field, with their trajectories being governed by a relativistic Lorentz force equation in the frame of the shock. The upstream fluid frame magnetic field is inclined at an angle $\Theta_{\rm Bf1}$ to the shock normal. Because the shock is moving with a velocity $\mathbf{u}(\mathbf{x})$ relative to the plasma rest frame, there is, in general, a $\mathbf{u}\times\mathbf{B}$ electric field in addition to the bulk magnetic field. Particle interactions with Alfvén wave and other hydromagnetic turbulence is modeled by using a phenomenological scattering of the charges in the rest frame of the plasma. The scattering precipitates spatial diffusion of particles along magnetic field lines, and to a varying extent, across them as well. The scatterings are also assumed to be quasi-elastic, an idealization that is usually valid because in most astrophysical systems the flow speed far exceeds the Alfvén speed, and contributions from stochastic second-order Fermi acceleration are small. The diffusion permits a minority of particles to transit the shock plane numerous times, gaining energy with each crossing via the coherent shock drift and diffusive first-order Fermi processes.

A continuum of scattering angles, between large-angle or small-angle cases, can be modeled by the simulation. In the local fluid frame, the time, δt_f, between scatterings is coupled (EJR90) to the mean free path, λ, and the maximum scattering (i.e. momentum deflection) angle, $\theta_{\rm scatt}$ via $\delta t_f \approx \lambda\,\theta_{\rm scatt}^2/(6v)$ for particles of speed $v\approx c$. Here the mean fee path is that for turning the particles around along field lines. Usually λ is assumed to be proportional to a power of the particle momentum p (see EJR90 and Giacalone, Burgess and Schwartz, 1992, for microphysical justifications for this choice), and for simplicity it is presumed to scale as the particle gyroradius, r_g, i.e. $\lambda=\eta r_g\propto p$. Simulation results are fairly insensitive to this choice. Moreover, the scattering law is generally assumed to be identical in both the upstream and downstream fluids. Departures from this can easily be accommodated, but usually incur only a change in the spatial scales for diffusion either side of the shock. The parameter η in the model is a measure of the level of turbulence present in the system, coupling directly to the amount of cross-field diffusion, such that $\eta=1$ corresponds to the isotropic *Bohm diffusion* limit, where the field fluctuations satisfy $\delta B/B\sim 1$. In the quasi-linear regime, $\delta B/B\ll 1$, one expects

that η should scale inversely as the variance of the field, i.e. $\eta \propto (\delta B/B)^{-2}$. In kinetic theory, η couples the parallel ($\kappa_\parallel = \lambda v/3$) and perpendicular ($\kappa_\perp$) spatial diffusion coefficients via the relation $\kappa_\perp/\kappa_\parallel = 1/(1+\eta^2)$ (Forman, Jokipii & Owens 1974; Ellison, Baring & Jones 1995). In parallel shocks, where the **B** field is directed along the shock normal ($\Theta_{\rm Bf1} = 0$), η has only limited impact on the resulting energy spectrum, principally determining the frequency of scattering and hence the diffusive spatial scale normal to the shock. However, in oblique relativistic shocks where $\Theta_{\rm Bf1} > 0$, the diffusive transport of particles across the field (and hence through the shock) becomes critical to retention of them in the acceleration process. Accordingly, for such systems, the interplay between the field angle and the value of η controls the spectral index of the particle distribution (Ellison & Double 2004; Baring 2004), a feature that is central to the interpretation of PWN spectra.

It should be remarked that this phenomenological description of diffusion in Monte Carlo techniques is most appropriate at high energies (where it is more or less commensurate with results from Monte Carlo codes that inject prescribed turbulence), and omits the details of microphysics present in plasma simulations such as PIC codes. In the injection domain at slightly suprathermal energies, the influences of complex turbulent and coherent electrodynamic effects become important, and will substantially modify the picture from that of pure diffusion that is presented here; such is the niche of PIC simulations. Note also that all subsequent simulation results presented here are obtained in the *test particle approximation*, where the accelerated population is not permitted to modify the overall MHD shock structure.

2.2 Results for Relativistic Shock Acceleration

Representative particle differential distributions $dN/dp \propto p^2 f(\mathbf{p})$ that result from the simulation of diffusive acceleration at mildly-relativistic shocks are depicted in Figure 1 (adapted from Baring 2009); the reader can survey Ellison & Double (2004), and Stecker, Baring and Summerlin (2007, hereafter SBS07) for $\Gamma_1 \gg 1$ simulation results that possess similar character to the parallel shock ($\Theta_{\rm Bf1} = 0^\circ$) examples in the Figure. These distributions are obtained just downstream of the shock and are measured in the shock rest frame. They are equally applicable to electrons or ions, and so the mass scale is not specified; presuming that the wind loss from pulsars is dominated by pairs, the mass scale is nominally m_e. A striking feature is that the slope and shape of the non-thermal particle distribution depends on the nature of the scattering. The often cited asymptotic, ultrarelativistic index of $\sigma = 2.23$ for $dN/dp \propto p^{-\sigma}$ mentioned above is realized only for parallel shocks with $\Theta_{\rm Bf1} = 0^\circ$ in the mathematical limit of small (pitch) angle diffusion (SAS), where the particle momentum is stochastically deflected on arbitrarily small angular (and therefore temporal) scales. As mentioned above, in practice, SAS results when the maximum scattering angle $\theta_{\rm scatt}$ is inferior to the Lorentz cone angle $1/\Gamma_1$ in the upstream region. In such cases, particles diffuse in the region upstream of the shock only until their velocity's angle to the shock normal exceeds around $1/\Gamma_1$, after

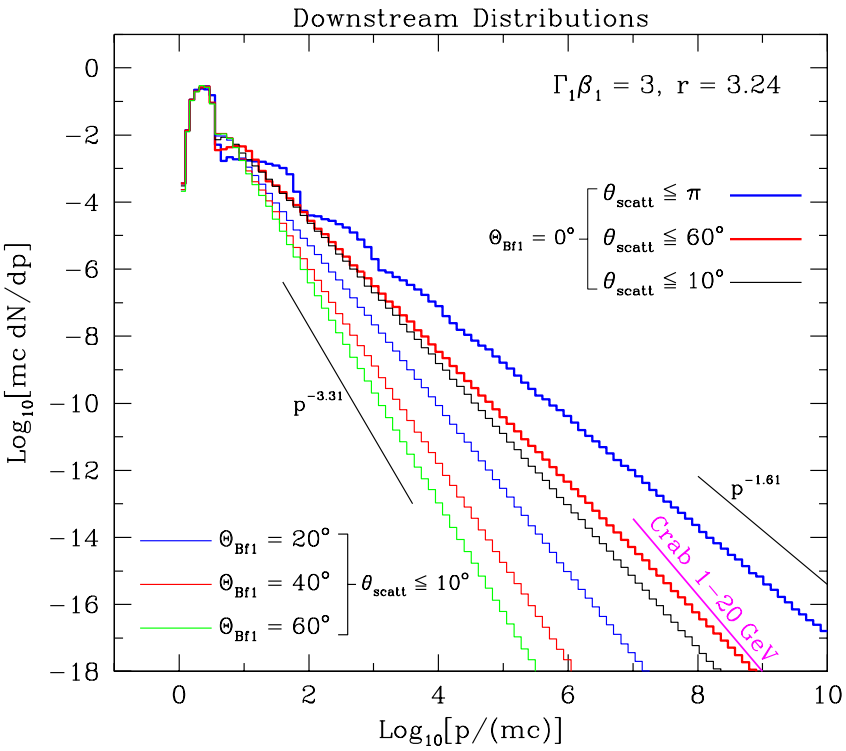

Fig. 1 Particle distribution functions dN/dp from mildly-relativistic shocks ($\Gamma_1\beta_1 = 3$, i.e. $\beta_1 = u_1/c = 0.949$) of upstream-to-downstream velocity compression ratio $r = u_{1x}/u_{2x} \approx 3.24$. Simulation results can be divided into two groups: parallel shock runs ($\Theta_{\rm Bf1} = 0°$, upper three histograms), and oblique, superluminal shock cases ($\Theta_{\rm Bf1} = 20°, 40°, 60°$, lower three histograms). Scattering off hydromagnetic turbulence was modeled by randomly deflecting particle momenta by an angle within a cone, of half-angle $\theta_{\rm scatt}$, whose axis coincides with the particle momentum prior to scattering; the ratio of the diffusive mean free path λ to the gyroradius r_g was fixed at $\eta = \lambda/r_g = 5$. The heavyweight lines (two uppermost histograms) are for the large angle scattering cases (LAS: $1/\Gamma_1 \ll \theta_{\rm scatt} \leq \pi$). All other cases constitute pitch angle diffusion (small angle scattering: SAS) runs, when $\theta_{\rm scatt} \ll 1/\Gamma_1$ and the distributions become independent of the choice of $\theta_{\rm scatt}$. All distributions asymptotically approach power-laws $dN/dp \propto p^{-\sigma}$ at high energies. For the two cases bracketing the results depicted, the power-laws are indicated by lightweight lines, with indices of $\sigma = 1.61$ ($\Theta_{\rm Bf1} = 0°$, $\theta_{\rm scatt} \leq \pi$) and $\sigma = 3.31$ ($\Theta_{\rm Bf1} = 60°$, $\theta_{\rm scatt} \leq 10°$), respectively. Also displayed is an indication of the index required to match *Fermi*-LAT > 1GeV observations for the Crab Nebula, assuming uncooled inverse Compton emission.

which they are rapidly swept downstream of the shock. The Figure indicates clearly that when the field obliquity $\Theta_{\rm Bf1}$ increases, so also does the index σ, with values greater than $\sigma \sim 3$ arising for $\Theta_{\rm Bf1} \gtrsim 50°$ for this mildly-relativistic scenario. This is a consequence of more prolific convection downstream away from the shock.

Figure 1 also shows results for large angle scattering scenarios (LAS, with $4/\Gamma_1 \lesssim \theta_{\rm scatt} \lesssim \pi$), where the distribution is highly structured and much flatter on average than p^{-2}. The structure becomes more pronounced for large Γ_1 (see Baring 2004; Ellison & Double 2004; SBS07, for details), and is kinematic in origin, where large angle deflections lead to fractional energy gains between unity and Γ_1^2 in successive shock crossings. Each structured bump or spectral segment corresponds to an increment of two in the number of shock transits (Baring 2004). For $p \gg mc$, they asymptotically relax to a power-law, in this case with index $\sigma \approx 1.61$. Intermediate cases are also depicted in Figure 1, with $\theta_{\rm scatt} \sim 4/\Gamma_1$. The spectrum is smooth, like for the SAS case, but the index is lower than 2.23. From the plasma physics perspective, magnetic turbulence could easily be sufficient to effect scatterings on this intermediate angular scale, a contention that becomes even more germane for ultrarelativistic shocks (SBS07). Note that there is a clear trend (e.g. see EJR90; Baring 2004; SBS07) of declining σ for higher Γ_1, the consequence of an increased kinematic energy boosting in collisions with turbulence.

The plot in Figure 1 includes an indication of the particle distribution index required to match the *Fermi* observations of the Crab Nebula. The *Fermi*-LAT spectral index in the 1–20 GeV range, corresponding to a putative inverse Compton signal, is $\alpha_\gamma = 1.64$ (see Abdo et al. 2010a, and specifically Figure 5 therein). In the case where this corresponds to the *in situ* accelerated population (i.e. the population is uncooled on the relevant timescales), one finds that $\sigma = 2\alpha_\gamma - 1 = 2.28$. Such a scenario is depicted by the "Crab 1–20 GeV" line in Fig. 1. In contrast, if inverse Compton cooling is sufficiently rapid as to define the total *Fermi* $> 1\,$GeV spectrum, then $\sigma = 2\alpha_\gamma - 2 = 1.28$. Thus, strongly-cooled IC models would suggest large angle scattering is active in the Crab Nebula termination shock, if it is *superluminal*.

Now for an important definition pertaining to the following discussion. The MHD phase space of relativistic shocks bifurcates neatly into two regimes. In general, Monte Carlo simulations "operate" in a shock rest frame named the normal incidence frame (NIF), where the upstream flow is directed along the shock normal (usually chosen to be the x-direction, a convention adopted here). In this frame, the upstream magnetic field is inclined to shock normal by an angle of $\Theta_{\rm Bs1}$. Due to relativistic aberration effects, generally $\Theta_{\rm Bs1} \neq \Theta_{\rm Bf1}$, with equality arising only in truly non-relativistic shocks. For many systems, there is also a shock rest frame called the de Hoffman-Teller (HT) frame (identified by de Hoffman & Teller 1950), which is obtained by a boost $u_{\rm 1HT} \equiv \beta_{\rm 1HT} c = u_{1x}/\cos\Theta_{\rm Bf1}$ along the magnetic field so as to bring the shock to rest. In this HT frame, there are no static electric fields, implying no $\mathbf{E} \times \mathbf{B}$ drifts parallel to the shock plane. *Subluminal* shocks are defined to be those where the HT flow speed $\beta_{\rm 1HT}$ corresponds to a physical speed, less than unity, i.e. the upstream field obliquity satisfies $\cos\Theta_{\rm Bf1} < \beta_{1x} \equiv u_{1x}/c$. When $\beta_{\rm 1HT} > 1$, the de Hoffman-Teller frame does not exist, and the shock is said to be *superluminal*. This division naturally demarcates a dichotomy for the gyrational characteristics of charges orbiting in the shock layer. Subluminal shocks permit many gyrational encounters of charges with the shock interface, and therefore also reflection of them into the upstream region. This implies efficient trapping (e.g

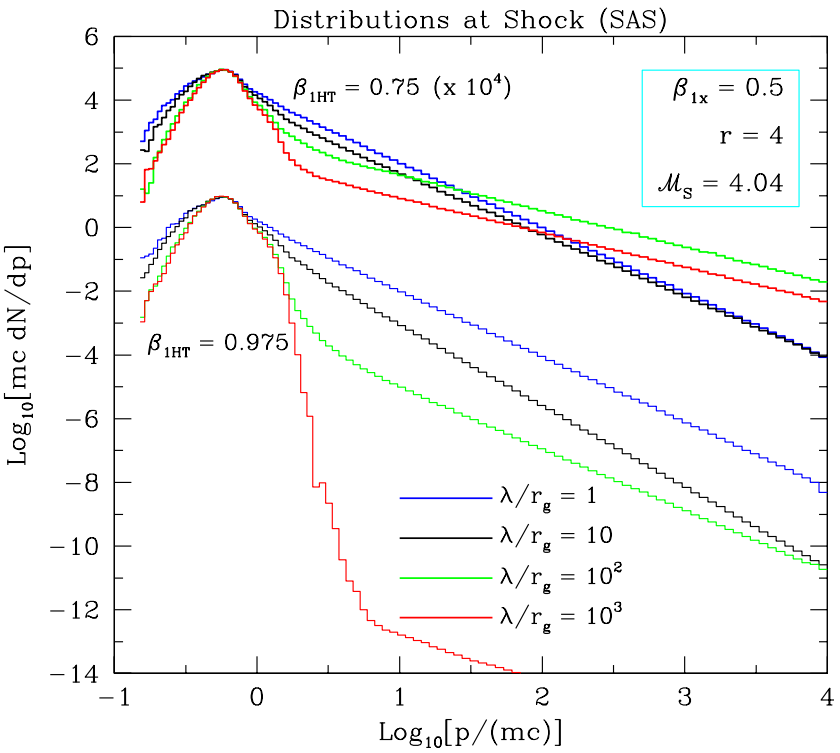

Fig. 2 Particle distribution functions dN/dp from mildly-relativistic sub-luminal shocks ($\Gamma_{1x}\beta_{1x} = 0.577$, i.e. $\beta_{1x} = u_{1x}/c = 0.5$) of upstream-to-downstream velocity compression ratio $r = u_{1x}/u_{2x} \approx 4$. Simulation results are depicted for two upstream fluid frame magnetic field obliquities, labelled by their corresponding de Hoffman-Teller frame upstream flow speeds $\beta_{1\rm HT} = \beta_{1x}/\cos\Theta_{\rm Bf1}$. These are in distinct groups of four: $\Theta_{\rm Bf1} = 48.2^\circ$ ($\beta_{1\rm HT} = 0.75$, multiplied by 10^4) for the upper four histograms, and $\Theta_{\rm Bf1} = 59.1^\circ$ ($\beta_{1\rm HT} = 0.975$) for the lower four histograms. Scattering off hydromagnetic turbulence was modeled by randomly deflecting particle momenta by an angle within a cone, of half-angle $\theta_{\rm scatt}$, whose axis coincides with the particle momentum prior to scattering; four different ratios of the diffusive mean free path λ to the gyroradius r_g were adopted for each $\Theta_{\rm Bf1}$. All results were for small angle scattering (SAS), when $\theta_{\rm scatt} \ll 1/\Gamma_1$ and the distributions become independent of the choice of $\theta_{\rm scatt}$. A low sonic Mach number $M_{\rm S}$ was chosen so as to effectively maximize the efficiency of injection from thermal energies. Adapted from Baring & Summerlin (2009).

see Baring & Summerlin 2009), and effective acceleration. In contrast, for superluminal shocks, in the absence of deflections of particles by magnetic turbulence, the convective power of the flow compels particles to rapidly escape downstream (e.g. Begelman & Kirk 1990), thereby suppressing acceleration. In such cases, particles sliding along the magnetic field lines would have to move faster than the speed of light in order to return to the upstream side of the shock. Such dramatic losses

from the acceleration mechanism can only be circumvented by strong cross field diffusion precipitated by large amplitude field turbulence fields (e.g. Jokipii 1987; Ellison, Baring & Jones 1995), i.e. essentially close to the Bohm limit.

The focus now turns to displaying the array of expectations for subluminal relativistic shocks. Principally, we will explore how the distribution index σ and injection efficiency depend on the effective frequency λ/r_g of scatterings, and the upstream field obliquity $\Theta_{\rm Bf1}$. Representative particle (lepton or ion) differential distributions dN/dp that result from the simulation of diffusive acceleration at mildly-relativistic shocks of speed $\beta_{1x} = 0.5$ are depicted in Figure 2. These distributions were generated for $\theta_{\rm scatt} \lesssim 10^\circ$, i.e. in the SAS regime. Results are displayed for two different upstream fluid frame field obliquities, namely $\Theta_{\rm Bf1} = 48.2^\circ$ and $\Theta_{\rm Bf1} = 59.1^\circ$, with corresponding de Hoffman-Teller frame dimensionless speeds of $\beta_{\rm 1HT} = \beta_{1x}/\cos\Theta_{\rm Bf1} = 0.75$ and 0.975, respectively. The distributions clearly exhibit an array of indices σ, including very flat power-laws, that are not monotonic functions of either the field obliquity $\Theta_{\rm Bf1}$ or the key diffusion parameter $\eta = \lambda/r_g$. Fig. 2 also emphasizes that the normalization of the power-laws relative to the low momentum thermal populations (and hence the injection efficiency $\varepsilon_{\rm inj}$) is a strongly-declining function of λ/r_g. Quantitatively, $\varepsilon_{\rm inj}$ drops from $0.1-0.2$ in the Bohm limit cases to less than 10^{-4} for $\lambda/r_g = 10^2$ when $\beta_{\rm 1HT} = 0.975$. This is a direct consequence of a more prolific convection of suprathermal particles downstream of the shock that suppresses diffusive injection from thermal energies into the acceleration process. Such losses are even more pronounced when $\lambda/r_g \geq 10^4$, to the point that acceleration is not statistically discernible for $\beta_{\rm 1HT} > 0.98$ runs with 10^4 simulated particles. This property is salient for the pulsar wind nebula context discussed below.

A parameter survey for diffusive acceleration at a typical mildly-relativistic shock is exhibited in Figure 3, where only the pitch angle diffusion limit was employed. The power-law index σ is plotted as a function of the de Hoffman-Teller frame dimensionless speed $\beta_{\rm 1HT} = \beta_{1x}/\cos\Theta_{\rm Bf1}$. It is clear that there is a considerable range of indices σ possible for non-thermal particles accelerated in mildly relativistic shocks. A feature of this plot is that the dependence of σ on field obliquity is non-monotonic. When $\lambda/r_g \gg 1$, the value of σ at first declines as $\Theta_{\rm Bf1}$ increases above zero, leading to very flat spectra. As $\beta_{\rm 1HT}$ approaches and eventually exceeds unity, this trend reverses, and σ then rapidly increases with increasing shock obliquity. This is the character of near-luminal and superluminal shocks evident in Fig. 2: it is caused by inexorable convection of particles away downstream of the shock, steepening the distribution dramatically. The only way to ameliorate this rapid decline in the acceleration efficiency is to reduce λ/r_g to values below around 10. Physically, this corresponds to increasing the hydromagnetic turbulence to high levels that force the particle diffusion to approach isotropy. This renders the field direction immaterial, and the shock behaves much like a parallel, subluminal shock in terms of its diffusive character. Charges can then be retained near the shock for sufficient times to accelerate and generate suitably flat distribution functions. This defines a second core property illustrated in Fig. 3: σ is only weakly dependent on $\Theta_{\rm Bf1}$ when $\lambda/r_g < 10$. Observe that the indication of the particle distribution

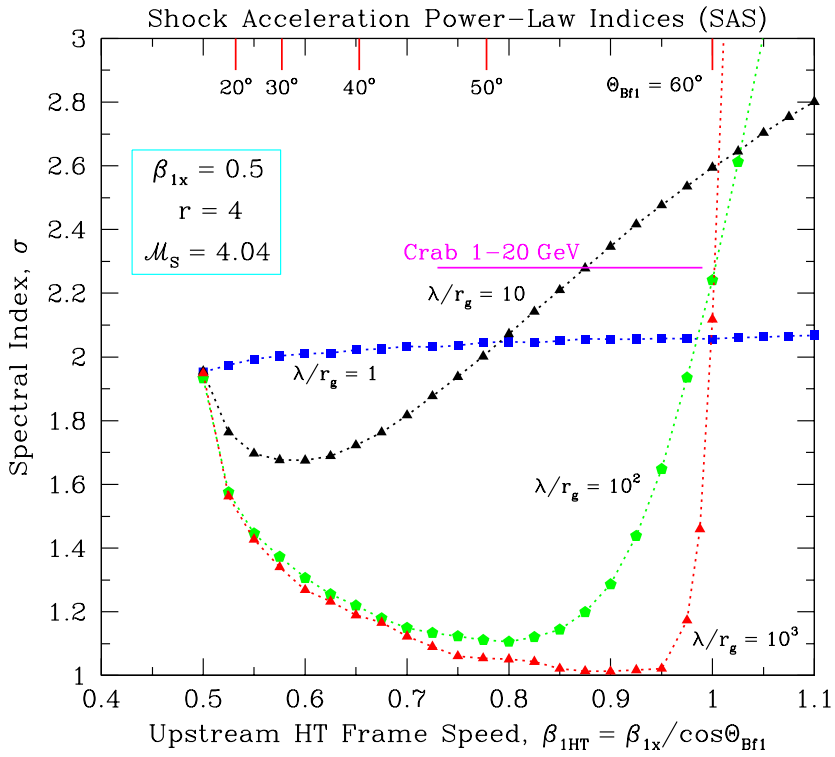

Fig. 3 Power-law indices σ for simulation runs in the limit of small angle scattering (pitch angle diffusion), for mildly-relativistic shocks of upstream flow speed $\beta_{1x} \equiv u_{1x}/c = 0.5$, and an MHD velocity compression ratio $r = 4$. The indices are displayed as functions of the effective de Hoffman-Teller frame upstream flow speed $\beta_{1\rm HT} = \beta_{1x}/\cos\Theta_{\rm Bf1}$, with select values of the fluid frame field obliquity $\Theta_{\rm Bf1}$ marked at the top of the panel. The displayed simulation index results were obtained for different diffusive mean free paths λ parallel to the mean field direction, namely $\lambda/r_g = 1$ (squares), $\lambda/r_g = 10$ (triangles), $\lambda/r_g = 10^2$ (pentagons), and $\lambda/r_g = 10^3$ (triangles), as labelled. The short heavyweight line indicates the approximate spectral index σ that is appropriate to match *Fermi*-LAT > 1GeV observations for the Crab Nebula, assuming uncooled inverse Compton emission is operable. Note that the indices for the $\beta_{1\rm HT} = 0.75,\ 0.975$ cases correspond to those of the distributions exhibited in Fig. 2.

index corresponding to *Fermi*-LAT observations in the 1–20 GeV range (for uncooled inverse Compton models; same as in Fig. 1) suggests low values of λ/r_g and proximity of the shock obliquity to the subluminal/superluminal boundary. This inference will be developed further below.

It is appropriate to identify briefly the reason why the distribution indices approach $\sigma \sim 1$ for subluminal shocks when $\lambda/r_g \gg 1$, i.e. the field is almost laminar. The origin of the extremely flat distributions with $\sigma \sim 1$ is in the coherent effect of

shock drift acceleration at the shock discontinuity, discussed extensively in Baring & Summerlin (2009). This phenomenon is due to the energy gain of charges when they repeatedly encounter $\mathbf{u}\times\mathbf{B}$ electric fields (in frames other than the HT frame) in gyrations straddling the shock discontinuity. Such gains are experienced between episodic upstream excursions as charges more or less retain gyrophases that permit reflection from the shock for long periods of time. Reducing λ/r_g, and thereby introducing extremely modest amounts of cross-field diffusion, disrupts this coherence, removes particles from the shock layer, and steepens the spectrum. It is not clear that astrophysical relativistic shocks can contain such low levels of turbulence as to access this academically interesting regime of phase space.

In concluding this overview of particle acceleration characteristics at relativistic shocks, it is noted that the results from these Monte Carlo simulations are in good agreement with those from other techniques, such as semi-analytic numerical solutions of the diffusion-convection equation, and also other Monte Carlo research initiatives. In particular, the artificially high choice of the compression ratio $r=4$ in Figures 2 and 3 was adopted to facilitate comparison with the semi-analytic work of Kirk & Heavens (1989). The reader is referred to Baring & Summerlin (2009) and Baring (2010) for more details on such simulation validation.

3 The Quasi-Perpendicular Pulsar Wind Termination Shock

The discussion now turns to lepton acceleration in pulsar wind termination shocks. While it is clear that their upstream flow speeds should be ultrarelativistic, it is unclear how fast they are. The historical paradigm of upstream bulk Lorentz factors $\Gamma_1\sim 10^5$ in the Crab Nebula has been promulgated from the seminal work of Kennel & Coroniti (1984). Pulsars can easily generate such bulk flows propagating out through the light cylinder, since the accelerating potentials in their gaps must energize primary electrons to at least $\gamma_e\sim 10^6-10^7$. This is true for both outer gap models (e.g. Cheng, Ho & Ruderman 1986; Romani 1996) or polar cap scenarios (e.g. Daugherty & Harding 1982; 1996) for the electromagnetic dissipation zone in gamma-ray puslars. If radiation reaction-limited curvature emission is what is principally responsible for the GeV emission seen in a host of *Fermi*-LAT pulsars (see the *Fermi* pulsar catalog compendium in Abdo et al. 2010b), then one can simply derive the relation $\gamma_e^3\lambda\!\!\!^{-}_{\rm c}/\rho_c\sim 2\varepsilon_{\rm MAX}/3$ for emission turnovers $\varepsilon_{\rm MAX}\sim 5\times 10^3$ (in units of m_ec^2) in the GeV band. Here ρ_c is the magnetic field curvature radius, which is some fraction of the light cylinder radius $R_{\rm lc}=Pc/(2\pi)$ for pulsar period P seconds. Also, $\lambda\!\!\!^{-}_{\rm c}=\hbar/(m_ec)=3.862\times 10^{-11}$cm is the electron Compton wavelength over 2π. With $10^6{\rm cm}<\rho_c<10^9\,{\rm cm}$, it is inferred that primaries assume Lorentz factors $10^6\lesssim\gamma_0\lesssim 10^7$ in a broad array of young to middle-aged pulsars.

However, pair cascading is rife in both the polar cap and slot gap/outer gap gamma-ray pulsar pictures. Much of the pair creation (magnetic one photon or conventional two-photon) occurs outside the gaps containing accelerating potentials. Several generations of pair production ensue, precipitating large pair multiplicities

$\eta_\pm \sim 10 - 10^4$ (e.g. see Daugherty & Harding 1982 for polar cap realizations, and Muslimov & Harding 2003 for slot gap results). Furthermore, similar values are obtained by De Jager (2007), who used the TeV inverse Compton flux in PSR B1509-58 and PSR B1823-13 to infer the total electron deposition integrated over the ages of their nebulae, thereby acting as a calorimeter for their pulsar pair multiplicities (see also Bucciantini, Arons and Amato 2010 for generally higher estimates for $\eta_\pm$). Simple energy conservation in the cascading process trades multiplicity for Lorentz factor, so that most of the emergent pairs propagating outwards from the gap region assume typical Lorentz factors of $\gamma_\pm \sim \gamma_0/\eta_\pm$. This then defines fiducial bulk Lorentz factors for the pair flow escaping towards the distant termination shock, so that for nebular modeling purposes $\Gamma_1 \sim 10^2 - 10^4$ may be more representative of the flow just upstream of the PWTS than the higher Kennel & Coroniti (1984) value. However, we note that since the wind is strongly magnetically-dominated at the light cylinder, mysteriously transitioning to a plasma-dominated flow at the termination shock (the so-called infamous σ problem), conversion of Poynting flux to bulk plasma kinetic energy is a distinct possibility for raising the value of Γ_1, perhaps taking advantage of magnetic reconnection in and near the current sheet.

The obliquity of the PWTS is less subject to such debate. If the termination shock is a fairly regular spatial structure, it must be highly oblique or an essentially perpendicular shock ($\Theta_{\rm Bf1} \sim 90^\circ$) in the equatorial wind zone, and also at much higher pulsar latitudes. Within the light cylinder, this follows from the winding up of the field in a classic Parker spiral, just like the solar wind termination shock (e.g. see Bogovalov, 1999, for a discussion of MHD structure in oblique rotators). Only directions outside the pulsar polar regions can possess more radial fields that permit the shock to be merely oblique, or even quasi-parallel. The actual solid angle (centered on the pulsar) portion of the PWTS that is quasi-perpendicular depends on the obliquity of the rotator, how the virtually rigid inner magnetospheric field morphology causally maps over to the field outside the light cylinder, and how the field geometry is modified by plasma loading. Yet it is in all probability large, regardless of whether Γ_1 is as high as 10^5 or as low as 10^2. From the MHD simulations of the Crab pulsar wind of Komissarov & Lyubarsky (2004), it is clear the the termination shock is non-spherical, being radially compressed in the polar zones. One can also entertain the possibility that the termination shock is slightly rippled, akin to what is an emerging paradigm for the solar wind shock based on the surprising magnetometer and energetic particle data acquired by the Voyager I and II spacecraft in the last few years. This can then permit localized regions of the PWTS to be subluminal or marginally superluminal. Or it can provide seeds for acceleration in a perpendicular shock zone from remote, but merely oblique shock environs. However, observational support for any such a conjecture is a long way off since it requires angular resolutions exceeding that of *Hubble* and *Chandra* to probe such PWTS geometry in bright PWNe like the Crab (see Hester et al. 1995 for *Hubble* and ROSAT images) and MSH 15-52 (see Gaensler et al. 2002 for *Chandra* imaging).

The content of the PWTS is generally presumed to be an electron-positron pair plasma. This derives from the leading models for dissipation in the pulsar magnetosphere: pairs are rife therein due to the relative ease of leptons being stripped from

the neutron star surface. Thermionic emission is possible in pulsars with higher surface temperatures. Moreover, if sufficiently intense parallel electric fields persist in the atmosphere, space-charge limited ion acceleration can proceed (Ruderman & Sutherland 1975; Arons and Scharlemann 1979). Such a prospect drove ideas that young neutron stars (Blasi, Epstein & Olinto 2000) and magnetars (Arons 2003) could act as accelerating sources of ultra-high energy cosmic rays. In the context of PWNe, baryonic loading of the wind that impacts the termination shock is possible, and inherently alters the character of the shock. Low energy charges then become subject to cross-shock potentials in the shock layer, since the inertial (i.e. gyrational) scales of the different species are widely disparate (e.g. see the discussion in Baring & Summerlin 2007). This can act to redistribute the thermal energy of the charges, possibly enhancing the injection and acceleration efficiency of leptons by tapping the inertia of the incoming thermal ions. Even if the pulsar wind is pair-dominated, it is still possible that the PWTS interface picks up ions from the proximate hydrogenic ejecta and feeds them into the acceleration process. Observational constraints on hadronic contributions to PWN gamma-ray emission are substantial. For example, the multi-zone models of multiwavelength emission in the Crab nebula of Atoyan & Aharonian (1996) indicate that pion decay emission from PWTS-accelerated protons colliding with cold ambient hydrogen lies comfortably below the inverse Compton signal in the 100 MeV – 1 TeV band, and is only likely to be detectable at energies $> 10\,$TeV. The flat spectrum and absence of any pion decay feature in the *Fermi*-LAT spectrum of the Crab (Abdo et al. 2010a) strongly suggest that the pair component of the PWTS is the most relevant. Given that both environmental and neutron star-driven baryonic loading are uncertain, and the observational mandate for treating hadronic emission in PWNe is limited, the discussion below will focus on pure lepton models for wind nebulae.

4 Connecting to PWN Observations

The emphasis now turns to making direct inferences on the pulsar wind termination shock environment and its lepton acceleration characteristics using the multiwavelength observations of nebular emission. This necessarily connects to the nonthermal power-law distribution indices σ. For the best known and most intensively-studied case of the Crab, the radio spectral index is quite flat at $\alpha_\gamma = 1.26$ (e.g. Wright et al. 1979), the X-ray index is steeper at $\alpha_\gamma \sim 2.1$ (see Weisskopf, et al. 2000; Atoyan & Aharonian 1996), the 1–20 GeV γ-ray spectrum has $\alpha_\gamma = 1.64$ (e.g. Abdo et al. 2010a) which slowly breaks to $\alpha_\gamma \sim 2.5$ above 1 TeV. The radio spectrum is not flat enough for synchrotron self-absorption, and no low frequency turnover that would be a signature of a minimum lepton Lorentz factor is observed. Accordingly, injection of pairs into the acceleration process must take place at energies below around 3–10 GeV. These characteristics are more or less representative of other PWNe: the radio index generally lies around 1.3 (see Gaensler & Slane 2006), and is flatter than the X-ray and TeV gamma-ray spectra, a nice synopsis of which

is provided in the recent review of Kargaltsev & Pavlov (2010). Even if effective radiative cooling is invoked at the maximum pair energies generating X-ray synchrotron emission, it becomes evident from these properties that the pair injection spectrum is *convex*, ranging from $\sigma \sim 1.5$ below around 30 GeV to $\sigma \sim 2.3$ well above 1 TeV (e.g. see Bucciantini, Arons & Amato 2010). As will become evident shortly, this is a significant constraint on diffusive acceleration at the PWTS.

We now identify the shock conditions required to generate these detected spectral indices, by considering shocks of higher speeds than in the previous Section. Representative spectral index results from Monte Carlo simulation runs are exhibited in Figure 4 (from Summerlin & Baring, in preparation), the $\beta_{1x} = 0.71$ portion of which mirrors those presented in Figure 3. When the Bohm limit of $\lambda/r_g = 1$ is realized, the non-thermal distribution index is approximately independent of the field obliquity. When the shock is superluminal, the index σ is a rapidly increasing function of $\Theta_{\rm Bf1}$. In subluminal regimes due to the powerful convective infleunces, when the field is laminar and $\lambda/r_g \gg 1$, very flat spectra can be realized because particles can be trapped in the shock layer and shock drift acceleration is very effective. Note also, that inefficient injection from thermal energies is then operative, as is exhibited in Fig. 2. The $\beta_{1x} = 0.95$ indices are those taken from Fig. 1 and indicate a moderate increase with obliquity in the superluminal regime. Such an increase is tempered relative to the $\beta_{1x} = 0.71$, $\lambda/r_g = 10$ situation largely because λ/r_g and the compression ratio are higher. The superluminal and ultra-relativistic $\Gamma_1 \approx 10$, $\Theta_{\rm Bf1} = 60^\circ$ results are possibly the most representative of the PWTS. They illustrate a significant sensitivity of σ to λ/r_g, yet the indices are lower than those for the shocks of lower speeds β_{1x}. This is caused by the increased kinematic energy gains in shock crossings for high Γ_1 for quasi-elastic interactions between charges and MHD turbulence in the shock layer.

The spectral indices observed for the Crab nebula in radio, X-ray and gamma-ray wavebands, as marked in Figure 4, offer clear constraints on the shock environment, if diffusive acceleration at the PWTS is the operable injection in PWNe. These can be taken to be more or less representative of the broader population of PWNe, though variations exist in the observational database. The flat radio (synchotron) spectra demand that the turbulence generate large mean free paths along **B** if the PWTS is subluminal. Shocks by their nature generate turbulence at levels that make this scenario unlikely (see the discussion in Baring & Summerlin 2009), disrupting the coherence that permits shock drift acceleration to operate prolifically. Given that the PWTS is very probably superluminal over most of its surface, the small angle scattering regime cannot supply flat enough acceleration distributions. Large angle scattering can though, as is evident in Fig. 1 and in Stecker, Baring & Summerlin (2007). This is not an unduly restrictive demand in ultra-relativistic shocks, since LAS is delineated by deflections $\theta_{\rm scatt} \gtrsim 1/\Gamma_1$, and it is easy to envisage that MHD turbulence in such shocks can spawn scattering angles of the order of a degree or so. It is this scenario that is the one most probably pertinent to the 1–30 GeV leptons.

The inverse Compton gamma-ray signal measured by the *Fermi*-LAT is probing leptons of energies in the TeV range. The spectroscopic demands are now different:

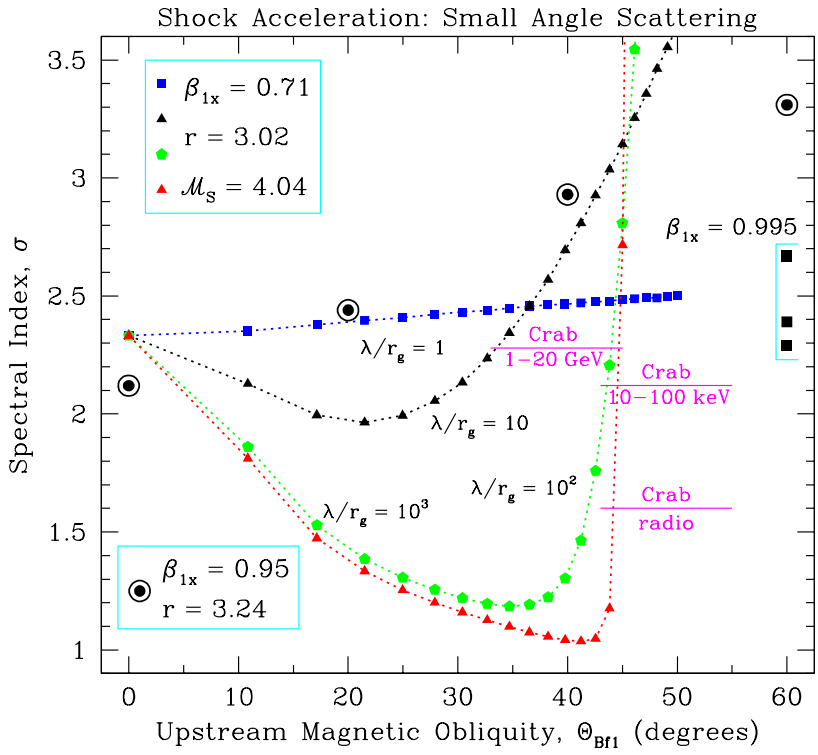

Fig. 4 Power-law indices σ for simulation runs in the limit of small angle scattering, for relativistic shocks of three different speeds. The indices are displayed as functions of the fluid frame field obliquity $\Theta_{\rm Bf1}$ (contrasting Fig. 3). Simulation data for the points connected by dotted lines were for an of upstream flow speed $\beta_{1x} \equiv u_{1x}/c = 0.71$, and an MHD velocity compression ratio $r = 3.02$; for these runs, obliquities $\Theta_{\rm Bf1} > 45^\circ$ constitute superluminal shocks. These index results were obtained for different diffusive mean free paths λ parallel to the mean field direction, namely $\lambda/r_g = 1$ (squares), $\lambda/r_g = 10$ (triangles), $\lambda/r_g = 10^2$ (pentagons), and $\lambda/r_g = 10^3$ (triangles), as labelled. Data for the higher shock speed ($\Gamma_1\beta_{1x} = 3 \Rightarrow \beta_{1x} \equiv u_{1x}/c = 0.949$) spectra displayed in Fig 1 (SAS only) are exhibited as circular points with dots centered therein. These are mostly superluminal and corresponded to $\lambda/r_g = 5$. The final subset of datapoints are the three filled squares grouped at $\Theta_{\rm Bf1} = 60^\circ$ for runs with $\Gamma_1\beta_{1x} = 10$ ($\beta_{1x} \approx 0.995$) with $r = 3.02$ (Summerlin & Baring, in preparation). These were obtained for $\lambda/r_g = 1, 3, 6$ ranging from the bottom to the top. As with previous Figures, short heavyweight lines are used to indicate the approximate spectral index σ that is appropriate to match Crab Nebula spectra in different wavebands: radio (presumed to be uncooled synchrotron), 10-100 keV X-ray (cooled synchrotron emission) and *Fermi*-LAT > 1 GeV observations (uncooled inverse Compton); see the text for a discussion.

the 1–20 GeV index can be supplied by either subluminal or superluminal shocks with SAS operating, provided that the turbulence is not far from the Bohm limit. LAS is also possible, but would require highly superluminal conditions to effect the requisite balance between large kinematic gains in shock-layer scatterings and

rapid convective losses downstream. The X-ray spectrum samples the highest energy electrons, in the super TeV range, that are subject to strong cooling (burn-off) over the nebular lifetime. Allowing for this modification, the inferences for the injected lepton spectrum at the PWTS are similar to those from the gamma-ray data. A broadband picture emerges that is highlighted in Atoyan & Aharonian (1996): the electron spectrum is convex (i.e. steepening) in the sense that σ is an increasing function of energy. This is not difficult to accommodate using the results from shock acceleration theory presented here, being modeled by a modest transition from LAS at low energies to Bohm-domain SAS at the highest pair energies. The portions of the PWTS driving this energization can be either superluminal or marginally subluminal. It is not hard to envisage turbulence that is slightly stronger at smaller scales than larger ones that might precipitate this LAS $\rightarrow$ SAS evolution with energy or Larmor radius in gyroresonant interactions. Yet in the near-term future, neither can observations resolve the angular scales to demonstrate such, nor can plasma simulations probe the wide dynamic ranges in lengthscales to validate such a scenario.

The simulation results presented here are for species of a single mass, obviously applying to pure pair shocks. It is natural to ask whether they might differ if the abundance of ions is significant. The answer must be deferred to future explorations of diffusive acceleration in hydrogenic plasma shocks. Yet it is expected that the the index results should be the same unless the turbulence generation is different when massive species are present. At energies below 1 GeV, the gyrational scales of protons and electrons of a given energy differ because the protons are at most only mildly-relativistic. This must lead to significantly different gyroresonant interactions for e^- and p. Furthermore, at these energies, charge separation cross shock potentials are anticipated to play a profound role in energy exchange between the two species (e.g. Baring & Summerlin 2007). These two contributions should provide substantial differences in injection efficiency between pair shocks and hydrogenic or electron-ion ones. This injection issue is clearly salient for the overall prediction of fluxes in different bands for PWNe. However, at energies well above 10 GeV, the gyro-scale of a charge of a given energy is independent of its mass, so that to leading order, turbulence generation and diffusion characteristics should be similar in this domain for relativistic $e^{\pm}$ and $e-p$ shocks.

Another question is whether or not the well-known non-linear spectral concavity encountered in non-relativistic shocks that efficiently accelerate charges (see Jones & Ellison 1991; Ellison & Double 2002; Baring 2004, and references therein) might compete with and preclude the spectral convexity that is demanded by the multi-wavelength observations. Such non-linear enhancements of high energy particles arise for distributions that have indices $\sigma \lesssim 2$, where these particles supply a sizeable portion of the total energy flux through the shock, and thereby modify the global MHD shock structure. While the radio observations in PWNe access this domain, the distribution convexity demanded by the gamma-ray and X-ray data must mute possible non-linear modifications, so that they should play a more minor role than in the non-relativistic shocks that illuminate supernova remnant outer shells.

5 Conclusions

This paper has outlined the key features of relativistic shock acceleration that pertain to lepton injection at termination shocks into pulsar wind nebulae. This shock is the most popular site for such injection, because (i) all pairs emanating from the pulsar that travel to the nebula must transit through this interface, (ii) it should be turbulent and therefore an efficient injector/accelerator, and (iii) the main characteristics of diffusive acceleration theory at shocks are fairly well understood. While it is quite possible that pre-acceleration can arise in magnetic reconnection zones between the pulsar light cylinder and the PWTS, such seed particles can be further energized at the shock to the point of masking the signatures of pre-acceleration. The historical models that developed the paradigm of the PWTS as an injector predate refined studies of relativistic shock acceleration over the last decade. As is evident here, these more recent studies support such a paradigm in being able to generate the requisite distribution indices to match the multiwavelength PWN observations without appealing to unlikely situations concerning turbulence in the shock layer. The key issue that remains unresolved by theory is how efficient injection arises from thermal energies in the PWTS. Does it occur for pure pair shocks, or is some baryonic loading necessary to precipitate prolific energization? Or, is a pre-acceleration seed required to set the diffusive processes at the shock active all the way to super-TeV energies? Addressing such questions will require more advanced simulations and theoretical analyses. The answer will illuminate the overall particle budget in pulsar wind nebulae, balancing radiation luminosity, non-thermal particle energetics, and the wind power from the pulsars that drives these fascinating systems.

Acknowledgements This research was supported in part by National Science Foundation grant PHY07-58158 and NASA grant NNX10AC79G.

References

1. Abdo, A. A., Ackerman, M., Ajello, M., et al. 2010a, ApJ, **708**, 1254–1267.
2. Abdo, A. A., Ackerman, M., Ajello, M., et al. 2010b, ApJ Supp., **187**, 460–494.
3. Achterberg, A., Gallant, Y A., Kirk, J. G. et al. 2001, M.N.R.A.S., **328**, 393–408.
4. Atoyan, A. M. & Aharonian, F. A. 1996, M.N.R.A.S., **278**, 525–541.
5. Arons, J. 2003, ApJ, **589**, 871–892.
6. Arons, J. & Scharlemann, E. T. 1979, ApJ, **231**, 854–879.
7. Ballard, K. R. & Heavens, A. F. 1992, M.N.R.A.S. **259**, 89–94.
8. Baring, M. G. 1999, in *Proc. of the 26th ICRC, Vol. IV* , pp. 5–8.
9. Baring, M. G. 2004, Nucl. Phys. B, **136C**, 198–207.
10. Baring, M. G. 2009, in *Proc. 6th Huntsville GRB Symposium*, eds. C. A. Meegan, N. Gehrels, & C. Kouveliotou (AIP Conf. Proc. 1133, New York) pp. 294–299. [astro-ph/0901.2535]
11. Baring, M. G. 2010, Adv. Space Res., in press. [astro-ph/1002.3848]
12. Baring, M. G. & Summerlin, E. J. 2007, Astr. Space Sci., **307**, 165–168.
13. Baring, M. G. & Summerlin, E. J. 2009, in "Shock Waves in Space and Astrophysical Environments," eds. X. Ao, et al., R. Burrows & G. P. Zank (AIP Conf. Proc. 1183, New York) pp. 74–83. [astro-ph/0910.1072]

14. Bednarz, J. & Ostrowski, M. 1998, Phys. Rev. Lett. **80**, 3911–3914.
15. Begelman, M. C. & Kirk, J. G. 1990, ApJ, **353**, 66–80.
16. Bell, A. R. 1978, M.N.R.A.S. **182**, 147–156.
17. Blasi, P., Epstein, R. I. & Olinto, A. V. 2000, ApJ, **533**, L123–L126.
18. Blasi, P. & Vietri, M. 2005, ApJ, **626**, 877–886.
19. Bogovalov, S. V. 1999, Astron. Astrophys., **349**, 1017–1026.
20. Bucciantini, N., Arons, J. & Amato, E. 2010, M.N.R.A.S., subm. [astro-ph/1005.1831]
21. Cheng K. S., Ho C. & Ruderman M. 1986, ApJ, **300**, 500–521.
22. Daugherty, J. K. & A. K. Harding 1982, ApJ, **252**, 337–347.
23. Daugherty, J. K. & Harding A. K. 1996, ApJ, **458**, 278–292.
24. de Hoffman, F. & Teller, E. 1950, Phys. Rev. D, **80**, 692–703.
25. de Jager, O. C. 2007, ApJ, **658**, 1177–1182.
26. de Jager, O. C. & Harding, A. K. 1992, ApJ, **396**, 161–172.
27. Double, G. P., Baring, M. G., Jones, F. C. & Ellison, D. C. 2004, ApJ, **600**, 485–500.
28. Ellison, D. C., Baring, M. G. & Jones, F. C. 1995, ApJ, **453**, 873–882.
29. Ellison, D. C. & Double, G. P. 2002, Astroparticle Phys. **18**, 213–228.
30. Ellison, D. C. & Double, G. P. 2004, Astroparticle Phys., **22**, 323–338.
31. Ellison, D. C., Jones, F. C. & Reynolds, S. P. 1990, ApJ, **360**, 702–714. (EJR90)
32. Forman, M. A., Jokipii, J. R. & Owens, A. J. 1974, ApJ, **192**, 535–540.
33. Gaensler, B. M., Arons, J., Kaspi, V. M. et al. 2002, ApJ, **569**, 878–893.
34. Gaensler, B. M. & Slane, P. O. 2006, Ann. Rev. Astron. Astrophys., **44**, 17–47.
35. Giacalone, J., Burgess, D., & Schwartz, S. J. 1992, in *ESA, Study of the Solar-Terrestrial System*, pp. 65–70.
36. Heavens, A. F. & Drury, L. O'C. 1988, M.N.R.A.S. **235**, 997–1009.
37. Hester, J. J., Scowen, P. A., Sankrit, R., et al. 1995, ApJ, **448**, 240–263.
38. Hoshino, M., Arons, J., Gallant, Y. A. & Langdon, A. B. 1992 ApJ, **390**, 454–479.
39. Jokipii, J. R. 1987, ApJ **313**, 842–846.
40. Jones, F. C. & Ellison, D. C. 1991, Space Sci. Rev., **58**, 259–346.
41. Kargaltsev, O. & Pavlov, G. G. 2010, to appear in proc. of "X-ray Astronomy 2009," held in Bologna, Italy (AIP, New York). [astro-ph/1002.0885]
42. Kennel, C. F. & Coroniti, F. V. 1984, ApJ, **283**, 694–709.
43. Kirk, J. G., Guthmann, A. W., Gallant, Y. A., Achterberg, A. 2000, ApJ, **542**, 235–242.
44. Kirk, J. G. & Heavens, A. F. 1989, M.N.R.A.S., **239**, 995–1011.
45. Kirk, J. G. & Schneider, P. 1987a, ApJ **315**, 425–433.
46. Kirk, J. G. & Schneider, P. 1987b, ApJ **322**, 256–265.
47. Kirk, J. G. & Skjæraasen, O. 2003, ApJ, **591**, 366–379.
48. Komissarov, S. S. & Lyubarsky, Y. E. 2004, M.N.R.A.S., **349**, 779–792.
49. Lyubarsky, Y. E. & Kirk, J. G. 2001, ApJ, **547**, 437–448.
50. Martins, S. F., Fonseca, R. A., Silva, L. O. & Mori, W. B. 2009, ApJ, **695**, L189–L193.
51. Medvedev, M. V., Fiore, M., Fonseca, R. A., et al. 2005, ApJ, **618**, L75–L78.
52. Morlini, G., Blasi, P. & Vietri, M. 2007, ApJ, **658**, 1069–1080.
53. Muslimov, A. G. & A. K. Harding 2003, ApJ, **588**, 430–440.
54. Niemiec, J., & Ostrowski, M. 2004, ApJ, **610**, 851–867.
55. Nishikawa, K.-I., Hardee, P., Richardson, G., et al. 2005, ApJ, **622**, 927–937.
56. Ostrowski, M. 1991, M.N.R.A.S. **249**, 551–559.
57. Peacock, J. A. 1981, M.N.R.A.S. **196**, 135–152.
58. Pétri, J. & Lyubarsky, Y. 2007, Astron. Astrophys., **473**, 683–700.
59. Rees, M. J. & Gunn, J. E. 1974, M.N.R.A.S., **167**, 1–12.
60. Romani, R. W. 1996, ApJ, **470**, 469–478.
61. Ruderman, M. A. & Sutherland, P. G. 1975, ApJ, **196**, 51–72.
62. Sironi, L. & Spitkovsky, A. 2009, ApJ, **707**, L92–L96.
63. Spitkovsky, A. 2008, ApJ, **682**, L5–L8.
64. Stecker, F. W., Baring, M. G. & Summerlin, E. J. 2007, ApJ, **667**, L29–L32. (SBS07)
65. Weisskopf, M. C., Hester, J. J., Tennant, A. F., et al. 2000, ApJ, **536**, L81–L84.
66. Wright, E. L., Harper, D. A., Hildebrand, R. H., et al. 1979, Nature, **279**, 303–305.